Quantum Electronics **33** (1) 57 – 68 (2003)

REVIEW

PACS numbers: 52.25.Jm; 52.25.Vy; 52.80.Tn; 61.43.Hv
DOI: 10.1070/QE2003v033n01ABEH002365

Fractal structures in a laser plume

N.E. Kask, S.V. Michurin, G.M. Fedorov

Contents

***Abstract*. A growth of fractal aggregates in laser plasma with a dispersion phase is discussed. The molecular compositions of saturated vapours produced by the effusion Knudsen method and by laser ablation are compared. A considerable attention is given to gas-like clusters. The formation of macroscopic structures during relaxation of the laser plasma and the role of dipole interaction in the aggregation of compact clusters are considered.**

Keywords: *optical discharge, fractal structures, dusty plasma, percolation.*

1. Introduction

The accepted model of formation of branched fractal microscopic structures from a vapour – gas phase is the model of diffusion-restricted aggregation. The aggregation in a discharge plasma is preceded by two processes: the formation of molecular associates and condensation of vapours. The condensation centres, around which liquid drops are formed, are predominantly ions. The associates grow during mutual collisions and become denser, which also results in the formation of liquid-phase nuclei. A model of a drop (compact cluster) is considered as a limiting case of an object having a maximum number of bonds in the cluster. Another limiting case is a model of an associate with a minimum number of bonds, when an atom interacts only with a pair of its nearest neighbours [1, 2]. Such an object is called gas-like because it cannot be characterised by a certain volume and density. The question of which of the models is more adequate for the description of the properties of clusters at high temperatures in a dense vapour – gas phase is of interest both for fundamental science (nonideal plasma and nucleation theory) and the modern technology for manufacturing new unusual structures. The role of associates in the formation of fullerenes and carbon nanotubes is obvious. An important role of associates in a discharge plasma is confirmed by experimental studies [3], which revealed stable branched macroscopic structures (dendritic long-lived filaments) whose elements are coupled by molecular bonds.

The details of processes proceeding in plasmas are not adequately studied so far. An optical discharge initiated and maintained by laser radiation near a target surface allows the study of a variety of media by varying external parameters in a broad range, making it possible to investigate the influence of the target material on the efficiency of formation of clusters and their aggregates in a high-density vapour – gas phase.

N.E. Kask, S.V. Michurin, G.M. Fedorov D.V. Skobeltsyn Research Institute of Nuclear Physics, M.V. Lomonosov Moscow State University, Vorob'evy gory, 119992 Moscow, Russia;
e-mail: nek@srd.sinp.msu.ru

Received 18 July 2002
Kvantovaya Elektronika **33** (1) 57 – 68 (2003)
Translated by M.N. Sapozhnikov

2. Vapour and plasma near the target surface

The process of evaporation of a target surface by laser radiation considered in many papers, reviews, and monographs (see, for example, [4 – 12] and references therein) is described by the following scheme. The regime of developed evaporation is realised at laser power densities

$$q \geqslant q_{\text{thr}} \approx \frac{k_B T_b}{\alpha 2(\chi t_p)^{1/2}}, \quad (1)$$

where α and χ are the absorption coefficient and the thermal diffusivity, respectively; t_p is the laser pulse duration; and T_b is the boiling temperature. As the power density increases, the target-surface temperature increases logarithmically, and almost entire absorbed energy is spent for evaporation. The rate u_a of an evaporation wave depends exponentially on the surface temperature T_0:

$$u_a = u_0 \exp\left(-\frac{T_0}{T_s}\right), \quad (2)$$

where u_0 is the sound speed in the target material; T_s is the evaporation heat per atom in kelvins. The pressure of saturated vapours near the target surface also depends exponentially on the temperature T_s:

$$P_s = P_0 \exp\left[\frac{\Lambda}{k_B}\left(\frac{1}{T_b} - \frac{1}{T_s}\right)\right], \quad (3)$$

where Λ is the latent heat of evaporation at the normal pressure P_0. As for the vapour flow velocity, their hydrodynamic flow is established in a Knudsen layer, which is adjacent to a surface being evaporated and has a thickness of a few mean free paths [13]. The vapour is cooled at the external boundary of the Knudsen layer. In the limiting case of the sonic flow (the Mach number $M = 1$) of a monatomic vapour, the temperature is lowered down to $T(M = 1) = 0.75T_s$. As a result, vapour becomes supersaturated, which leads to its condensation. Although the front of formation of 'viable' nuclei can be separated from the surface being evaporated by tens and hundreds of mean free paths, condensation also takes place at the initial stage of the expansion. The energy released in this case affects the parameters of vapour at the external boundary of the Knudsen layer. In particular, the temperature is increased and, hence, the vapour becomes less supersaturated. Polyatomic vapour can remain unsaturated at the boundary of the Knudsen layer even when the Mach number is close to unity. Nuclei will be formed mainly at the subsequent stages of the plasma expansion due to the adiabatic expansion of the flow of evaporated matter.

The near-surface plasma induced and maintained by laser radiation is usually classified in accordance with processes proceeding in it [14–16]. The erosion and thermal decomposition of the target material lead to the formation of a vapour–gas flow whose weak electron–ion component is determined by the ionisation equilibrium. The extinction of laser radiation in an erosion plume is caused by bremsstrahlung absorption at temperatures of the order of 10^4 K (see, for example, [17]) and by the appearance of a drop fraction at the plasma temperature no less than a few thousands of kelvins. In the latter case, according to [18, 19], the concentration of particles of size of the order of 0.1 μm changes from 10^{10} to 10^{12} cm^{-3}. The plume is semitransparent for incident laser radiation, and the vapour temperature in it is close to the boiling temperature of the target material ($\sim 10^3$ K). In the emission spectrum, emission lines of atoms and emission bands of molecules dominate [14, 20]. The laser energy is predominantly absorbed at the target surface, where a cavern is produced. Along with evaporation, the melt is removed from the cavern due to a thermocapillary motion [21], whose intensity depends on the spatial variations in the surface tension.

Plasma can appear and develop without the formation of a crater on the target surface. Various mechanisms facilitating the low-threshold breakdown were considered in papers [22–28]. These mechanisms are the evaporation of the target material [23], the evaporation of surface defects [26, 27], and the thermal explosion of microcusps [28]. The low ionisation potential of metal vapours and the absence of the electronic energy losses for excitation of the vibrational molecular levels facilitate the development of an avalanche breakdown. Depending on the experimental conditions and radiation parameters, either a near-surface optical discharge can be produced near the target or a light combustion wave propagating towards laser radiation. The velocity of the wave front is determined by the mechanism of energy transfer to surrounding cold layers. For light fluxes of a moderate intensity, energy transfer occurs due to thermal conductivity [29, 30]. The plasma of the optical discharge in gases has a high temperature (15000–20000 K), high degree of ionisation (approaching a complete single ionisation), and has the absorption coefficient for laser radiation which screens the surface.

An optical discharge can be also produced in the target vapours. A comparatively low ionisation potential of vapours reduces the plasma temperature compared to the temperature in gas discharges. Due to the surface screening, the discharge in vapours can be nonstationary [16] because vapour is absent in front of the wave and, unlike the gas discharge, the propagation medium is absent. As a result, when the laser power density is low enough, the velocity of the discharge propagation towards the incident radiation is limited by the velocity of the flow of target-material vapours. The emission spectrum exhibits mainly the emission lines of ions [31]. As the power density of the light flux increases, the passage from the discharge in vapours to the gas discharge, like the passage from an erosion plume to the vapour (gas) discharge occurs sharply.

Because the gas-breakdown threshold depends on the gas density [30], a change in the discharge regime can also occur when the external pressure is increased. We are not aware of a systematic study of a low-threshold breakdown depending on the surrounding gas pressure. The experimental data on gas (nitrogen) breakdown at elevated pressures near target surfaces (molybdenum, stainless steel) are presented in papers [32–34]. It is assumed that, in the range from 30 to 100 atm and at power densities $10^6 - 10^7$ W cm^{-2}, a light combustion wave propagates in the gas after its breakdown. A plasma region is formed behind the wave front, which virtually completely screens the target from the incident laser radiation.

3. Plasma containing a dispersion phase

Plasma with a condensed dispersion phase is a weakly ionised gas containing solid or liquid particles of size 10^{-9}–10^{-6} m. Such particles are present almost in any low-temperature plasma due to the condensation of a vapour–gas phase or sputtering of electrodes, target, etc. The presence of particles affects all the main parameters of the plasma and its transport and optical properties. For example, particles of micron and submicron sizes efficiently capture electrons, acquiring a charge as high as $10^3 - 10^5 e$

per particle (where e is the elementary charge). If the concentration of particles is sufficiently high, the electron density decreases noticeably. Particles can capture virtually all the negative charge of the plasma [35, 36], thereby changing substantially its conductivity. To maintain a discharge at an invariable ionisation rate, the electron temperature should increase, which results in a more intense optical emission.

Depending on whether particles in the plasma are stable or, on the contrary, grow and evaporate, the plasma is called the dusty or cluster plasma [37]. In the cluster plasma, which exists at relatively high pressures and high temperatures, processes involving atoms (condensation and evaporation) play the dominant role. Ions with a comparatively low degree of ionisation prove to be the condensation centres. The three-particle character of the formation of diatomic molecules inhibits the nucleation of clusters at low pressures. The important parameters of the cluster plasma are the pressure of saturated vapour and, hence, the temperature of the cluster surface. The atoms of a buffer gas and the plasma electrons play a dominant role in the thermal balance. For this reason, the cluster surface is heated up to the temperature that is higher than the gas temperature but is lower than the electron temperature. An individual sufficiently large cluster is described with the help of the liquid drop model [37, 38]. In particular, when the number n of atoms forming a cluster is large ($n \geqslant 100$), the volume and surface parameters of the appropriate liquid medium can be used. On the contrary, models based on the properties of a continuous medium cannot be applied to describe small clusters ($n \sim 30$). If the cluster temperature proves to be lower than its melting temperature, which depends on the cluster size, then the cluster is solidified. The binding energy of atoms in the surface layer of a solid cluster is not a monotonic function of its size and reaches a maximum for closed configurations [39].

In the theory of nucleation [40], a concept of a nucleus, representing a critical cluster for which the probabilities of the attachment and evaporation of atoms coincide, is introduced. For clusters of lower sizes, the rate of attachment is lower than the evaporation rate. The radius of a critical cluster is determined by the expression [41]

$$r_{\mathrm{cr}} = \frac{2\gamma v}{k_{\mathrm{B}} T \ln S}, \tag{4}$$

where $S = N/N_{\mathrm{s}}(T)$ is the degree of vapour supersaturation; N is the density of vapour atoms; $N_{\mathrm{s}} = P_{\mathrm{s}}/k_{\mathrm{B}}T$ is the vapour density in a saturated vapour; v is the volume occupied by an atom in a condensed phase; an γ is the surface tension coefficient. For a laser plasma produced upon evaporation of metals, we have $S \sim 2$ and $r_{\mathrm{cr}} \sim 1$ nm ($n \sim 1000$) [41].

Due to the attachment of electrons and ions, clusters acquire a charge of a few e [37, 42]. In the case of a conducting cluster, its total surface charge changes by unity. In the case of a dielectric particle, charged centres are formed at its surface, which are not necessarily of the same sign. Coagulation upon collisions of neutral or oppositely charged clusters determines the later stage of nucleation, when a fraction of substance in the vapour state becomes comparatively small.

The dusty plasma is studied, as a rule, at low pressure when the electron temperature greatly exceeds the ion temperature. The latter circumstance provides the negative sign of dust particles, which is proportional to their size. The energy of the Coulomb interaction between charged dust particles can noticeably exceed the energy of their thermal motion [43]. As a result, a strongly bound Coulomb liquid [44, 45] and a Coulomb crystal [44, 46] can be produced. The ordered dusty structures were observed in electrostatic traps [44], the near-cathode region of a high-frequency discharge [43], and in standing stratas of the positive column of a glow discharge [47].

Several evolution studies of the dispersion phase in the plasma of a radio-frequency discharge in the $SiH_4 : Ar = 5 : 95$ mixture ($P = 120$ mTorr) were distinguished using the methods of mass spectrometry [48] and photodetachment [49] produced by laser radiation. At the initial stage, negative ions are formed. Then, macromolecular nanostructures are formed, which have a comparatively small negative charge. The next stage, which proceeds for a time period from a few hundreds milliseconds to a few seconds, is of a coagulation nature. At the beginning of this stage, compact nanoclusters are formed. The electron microscopy shows [50] that these clusters are not spherical but rather resemble a structure of close-packed smaller spheres. The formation of larger particles with a larger negative charge is accompanied by a decrease in the electron density in the plasma and an increase in the electron temperature. Having reached a critical size, the particles leave the discharge region because the ion drag force and the thermophoretic force, ejecting particles from plasma, quadratically depend on the particle size, whereas the electrostatic force, which pulls particles into the discharge, depends linearly on the particle size. As a result, a cavity is formed in the plasma, which does not contain large particles [45, 46].

4. Macromolecules in a saturated vapour

Therefore, macromolecules can appear initially in the plasma. In this connection, it is of interest to determine the molecular composition of the saturated vapour obtained, for example, by the effusion Knudsen method [51], in which a narrow gas-dynamic jet ($\lambda \ll d$, where λ is the mean free path of atoms and d is the jet diameter) is used to form gas-like clusters. An increase in the velocity of translational motion and a decrease in the gas temperature cease when the gas-dynamic expansion regime passes to the molecular regime ($\lambda \gg d$). This usually occurs after the gas flow has passed the distance equal to a few nozzle diameters, and the gas density has decreased down to $10^{14} - 10^{12}$ cm^{-3}. During the molecular regime, the clusters, which have appeared and were grown at the previous expansion stage, lose the possibility of a further growing because of the absence of collisions (the so-called quenching effect). The typical time of this process is $10^{-7} - 10^{-6}$ s [52]. The component composition of a vapour–gas flow in the molecular regime is analysed by mass spectrometry.

A combination of the effusion method and mass spectroscopy made it possible to determine the molecular composition of the saturated vapour for most elements of the periodic system and basic inorganic compounds [51]. It was found that all metals evaporate in the form of atoms, while the fraction of dimer molecules changes from 10^{-1} to 10^{-7}. The composition of the saturated vapour for nonmetals proved to be more complicated. Thus, a set C_n of molecules was found for carbon, where n takes values from

2 to 10, with a maximum for $n = 3$. A similar picture was observed for elements of the six group (S, Se). In the saturated vapour of alkali-metal halides, the main component is a monomer, while the content of dimers can achieve 50 %. Oxides of metals of the first and second groups dissociate upon evaporation with the formation of a metal and oxygen. For the fourth-group oxides, the MeO monoxide and its polymers are the main components of the vapour, the degree of polymerisation being increased in passing from silicon to lead [53].

It was shown already in the first experiments on laser heating of carbon [54] that the degree of polymerisation of molecules in the vapour flow is greater ($n = 14$) than that in the effusion method. Later, a set C_n of molecules with $n \leqslant 24$ was detected upon laser evaporation of graphite in vacuum. Even greater degree of polymerisation ($n > 100$, where n in an even number) was obtained using the gas-dynamic jet method and laser evaporation [55]. Maxima in the spectrum were observed for $n = 60$ and 70; they were made narrower by increasing the residence time of molecules in the collision region [56]. The carbon molecules with $n \leqslant 7$ had a linear structure, and those with $n = 11 - 28$ had a cyclic structure. Spherically closed structures (fullerenes) dominated beginning from $n \geqslant 50$. Experiments [55, 56] also demonstrated the important role of a buffer gas, whose presence increases the polymerisation efficiency. Note that laser ablation causes a large degree of polymerisation in the case of oxides as well. For example, after irradiation of yttrium oxide by a single laser pulse, the $(Y_2O_3)_n(YO)^+$ ions with n varying from zero to 18 were detected by mass spectroscopy [57]. A further increase in the degree of polymerisation was obtained in single-layer carbon nanotubes, which represent folded graphite layers [58]. The length of such tubes of diameter of the order of one nanometer was a few hundreds of micrometres. One of the methods for manufacturing nanotubes is laser ablation in the buffer-gas atmosphere [59]. Except single-wall tubes, multiwall carbon nanotubes with the number of concentric layers achieving a few tens were also obtained.

5. Formation of nanoclusters

The typical duration of the process of formation of clusters by the methods of effusion [51] and laser ablation [60] is determined by the quenching time and is $10^{-7} - 10^{-6}$ s. It is interesting to compare the results obtained by these two methods. Note that in the Knudsen method, vapour is expanded to vacuum, whereas most of the experiments with cluster plasma (including laser ablation) are performed in the buffer-gas atmosphere. The buffer gas noticeably increases the clustering efficiency, absorbing the excess energy released upon condensation. Various gas-dynamic processes in the surrounding gas complicate the problem compared to the case of the expansion of matter to vacuum. Most of the theoretical papers devoted to laser ablation considered the condensation and formation of a cloud upon the expansion of vapour to vacuum.

These phenomena were first analysed in paper [61]. Condensation processes in a cloud formed upon laser ablation of substance in vacuum were simulated in papers [60, 62, 63]. It was shown that the theoretical model proposed in [61] well describes the experiment [64] on ablation of silicon in the helium atmosphere ($P = 4$ Torr). It was predicted for Ge, Si, and C that clusters of a critical size appearing for 50 ns in vacuum contain 16, 18, and 20 atoms, respectively [62]. The mass spectroscopy study [65] showed that the smallest compact silicon clusters consisting of 30 atoms appear in the buffer-gas atmosphere only after ~ 200 ns.

We can assume, following the discussion in Section 4, that macromolecular objects are formed at the initial stage of clustering, which are similar to 'gas clusters' obtained by the Knudsen method [51] and in a high-frequency discharge [48]. Later, these structures acquire a compact shape of a liquid drop or a solid particle. This is confirmed by experimental studies of the delay of the photoluminescence signal [66], which is observed in silicon only in a solid state [67], and also by the study of the fragmentation of initial structures caused by laser irradiation [68]. The time of formation of compact clusters, which depends on the pressure and type of a buffer gas, proved to be of the order of 1 ms [66].

When ablation is performed in a buffer gas ($P \sim 1$ atm), condensation continues as long as the density of free atoms in vapour is nonzero. The characteristic time τ of the condensation process and the number n of atoms are described by the expressions [37]

$$\tau \propto \frac{1}{k_0 N_a}\left(\frac{k_0}{K N_a}\right)^{1/4}, \quad n \propto (k_0 N \tau)^3 \propto \left(\frac{k_0}{K N_a}\right), \tag{5}$$

where $K \sim 10^{-33}$ cm^6 s^{-1} is the rate constant of the three-body process of formation of diatomic molecules, which are the condensation centres; $k_0 = \pi r_{cl}^2 (8T/\pi m)^{0.5} \sim 10^{-11}$ cm^3 s^{-1} is a constant determining the rate of attachment of atoms to a cluster of radius r_{cl}; m is the mass of vapour atoms; and $N_a \sim 10^{19}$ cm^{-3} is the density of buffer-gas atoms. As a result, we obtain the average number of atoms in a cluster $\bar{n} \sim 10^2$ for $N\tau \sim 10^{12}$ cm^{-3} s.

If the laser irradiation time t_p greatly exceeds τ, then the characteristic size of a cluster can be estimated from the expression [37]

$$n \propto \left(\frac{k_0}{K N_a}\right)^{5/8} \frac{t_p}{\tau}. \tag{6}$$

The heating of a material produced by laser radiation is, as a rule, nonuniform. The gradients of temperature and vapour density produced in this case are directed towards each other. According to the expression $P = N k_B T$, we have [37]

$$\frac{\Delta N}{N} = -\frac{1}{2}\frac{\nabla T}{T} = -\frac{\nabla P}{P}. \tag{7}$$

Because the density of atoms and the degree of supersaturation in cold regions are higher, while the evaporation rate is higher in hot regions, clusters are accumulated in more cold peripheral plasma regions. When the total density of vapour atoms contained in clusters $N_b = nN_{cl}$ (where N_{cl} is the number density of clusters) greatly exceeds the vapour density, a further growth of clusters occurs according to the coagulation mechanism. In this case, the average number of atoms in a cluster is described by the expression

$$\bar{n} = 3.5(N_b k_0 t)^{1.2} \quad (N_b k_0 t \gg 1). \tag{8}$$

By equating N_b to the concentration of the evaporated material ($\sim 10^{19}$ cm^{-3}), we obtain that the characteristic size of the clusters by the end of a 10-ms laser pulse will be ~ 10 nm ($n \sim 10^5$). This corresponds to the characteristic size of compact particles from which fractal structures are formed upon laser evaporation [69, 70].

6. Charge of clusters

The surface of any body in a contact with a plasma becomes charged. The high temperature and intense emission of the plasma cause thermal and photoelectronic emission from the surface, resulting in the accumulation of a positive charge on the surface. When the plasma temperature does not exceed 1000 K, the charge is determined by a balance between the flows of positively and negatively charged plasma particles coming to the surface. Because electrons are more mobile, having acquired a negative charge, the surface begins to attract positive ions and repel electrons until a stationary negative charge is established. The surface layer of the plasma, being polarised, restricts the action of the Coulomb force of the accumulated charge. The screening is characterised by the Debye length.

A sufficiently large isolated particle ($a \geqslant 10$ nm) behaves in the plasma as a spherical capacitor with the capacitance $C \approx 4\pi\varepsilon_0 a$ and the charge $Z_a = C/V(a)$, where $V(a)$ is the floating potential depending on the temperature and mass of plasma particles (T_e, T_i, m_e, m_i). The particle charge is proportional to its radius. Each particle is surrounded by the Debye sphere with a charge of the opposite sign, which is characterised by the screening length. The estimate [49] of the accumulated charge for typical parameters of the low-pressure plasma ($P \sim 10$ Torr) with a low gas temperature ($T \sim 300$ K) gives one elementary charge per one nanometer of the particle radius. Therefore, a particle of micron size in such a plasma acquires a charge of the order of $1000\,e$.

Nanoparticles can be considered as large molecules, and the process of charge accumulation for them can be described in terms of recombination and electron detachment rather than in terms of a balance of flows. A charge accumulated on such particles does not exceed usually several e, and they are never in the stationary state; their charge fluctuates and is described by statistical methods [71].

When the concentration of large charged particles is sufficiently high, the negative charge per particle decreases due to the overlap of Debye spheres. In the limit of a very high number density N_p of particles, the particles accumulate almost all electrons, and a charge per particle is

$$Q_p = \frac{n^+}{N_p}, \tag{9}$$

where n^+ is the ion density. Note that the stationary charge is established for $\sim 10^{-10}$ s [49, 72].

7. Formation of fractal structures during plasma relaxation

The formation of fractal structures after plasma relaxation was observed upon the electric explosion of conductors [73], evaporation of metals heated to high temperatures [74], arc discharge and combustion [75], laser evaporation [69, 70, 76], and plasma sputtering [77]. Fractal aggregates produced in a plasma plume were deposited on a substrate and were studied by electron microscopy. A separate fractal cluster has a micron size and consists of nanometer particles (3 – 10 nm). The distribution of the matter density in the cluster is characterised by the fractal dimensionality d_f, which depends in the general case on the experimental conditions and the mechanism governing the cluster growth [78]. Two models of the fractal growth in a gas phase are more widely used: the diffusion-limited aggregation in the particle–cluster system ($d_f = 1.6 \pm 0.07$ [73]) and cluster–cluster aggregation ($d_f = 1.77 \pm 0.03$ [79]). The aggregation in solutions is more often restricted by the rate of a chemical reaction rather than by diffusion; as a result, the average density of matter in the cluster proves to be higher and its fractal dimensionality is higher ($d_f = 2.02 \pm 0.06$ [80]). Gels also can be formed in solutions [81], when a bound macroscopic structure consisting of fractal structures is produced due to sol–gel transitions stimulated by a chemical reaction. The dimensionality of these clusters coincides with that of critical percolation clusters, which depends only on the dimensionality of the Euclidean space: $d_f = 1.80 \pm 0.05$ on a surface and 2.35 ± 0.05 in a volume [82]. These values of d_f were obtained experimentally and are in good agreement with model calculations based on the approximation of solid spheres, i.e., in the absence of interaction between particles.

Experiments showed that the fractal dimensionality of structures obtained from a vapour–gas phase proved to be lower ($d_f = 1.4 \pm 0.2$ [42, 70]) and depended on an external electric field [42]. The model of diffusion-limited aggregation was substantially modified [83–86] by introducing the dipole–dipole interaction between particles whose dipole moment can be induced by an external electric field [85, 86]. According to calculations [84, 85], as the interaction energy increases, the fractal dimensionality decreases from ~ 1.7 down to ~ 1.1 and from ~ 2.46 down to ~ 1.37 in the two-dimensional and three-dimensional cases, respectively. In this modified model, the parameter p^* is introduced, which characterises the relation between the dipole interaction and thermal energy

$$p^* = \frac{\mu^2}{d_\mu^3 k_B T}, \tag{10}$$

where μ is the dipole moment of a particle and d_μ is the distance between dipoles. If $p^* < 1$ (high temperatures and weak interaction), then usual branched fractal clusters are formed. If $p^* > 1$ (low temperatures and strong interaction), then particles are aligned to form linear chains. Note that such a behaviour of ferromagnetic particles was discovered and interpreted earlier in paper [87].

As fractal clusters are accumulated, macroscopic structures such as aerogel [82], fractal structures [72, 88], and fractal filaments [70, 89] are formed. The silicon dioxide aerogel is the most thoroughly studied macroscopic fractal object [90, 91]. The main element of this macrostructure is a fractal cluster, and structures reveal fractal properties at scales that are lower than its size (no more than 1 μm). At greater scales, macrofractals possess the properties of a homogeneous system. Note that the dimensionality of an isolated fractal cluster deposited from a gas phase averages ~ 1.8, whereas $d_f = 2.4 \pm 0.2$ in the aerogel structure [91].

Cluster deposited on a substrate produce fractal layers. The distribution of material in them depends on the cluster

parameters (thermal energy, size, charge, dipole moment, dimensionality, etc.), their number density, and the properties of the surface itself. The model experiment describing the deposition of clusters on a substrate, their diffusion over the substrate surface and aggregation to the structures existing before was performed in paper [92]. It is shown that the morphology of a fractal layer depends on the relation between the system size L and the characteristic scales (diffusion length L_1 and average distance L_2 between the growing structures) and can correspond to different models of the structure growth. Thus, the morphology of a cluster produced during the diffusion-limited aggregation is realised in the case of weak particle flows and a small size of the system compared to the diffusion length ($L < L_1$). The model of cluster–cluster aggregation is realised for weak flows and small diffusion length ($L_1 < L < L_2$). The percolation cluster model corresponds to structures formed in the case of strong flows and large systems ($L > L_2$). The presence of the dipole moment of the particles being deposited and the long-range interaction between them result in the appearance of ordered structures (chains) at low temperatures [88, 93].

Fractal filaments appear due to the aggregation of fractal clusters in the presence of an electric field (~ 100 V cm^{-1}) [70]. The field causes the reorientation of microstructures, their directional aggregation and thickening inside a filament due to restructuring – the dissociation of weak bonds and formation of new stronger bonds. It was shown [89] that a fractal filament can be formed due to a percolation transition in an ensemble of fractal aggregates (clusters) if their concentration exceeds some critical quantity. The transition occurs during a comparatively short time interval (no longer than 1 s) compared to the accumulation period (~ 1 min). In the case of evaporation of textolite by laser radiation, a filament of length ~ 1 m and thickness ~ 1 mm was formed from carbon black particles [89].

In experiments with a radio-frequency discharge in a dusty plasma [77], fractal aggregates of size no more than 10 μm produced due to electrode sputtering were detected. Fractals behave as compact dusty particles, which accumulate an electric charge and, having reached a certain concentration and size, move to the discharge periphery. As a result, a cavity with sharp boundaries and enhanced emission is formed inside a cloud of dusty particles. Dusty particles observed in these experiments have a size of ~ 0.5 μm and a charge of $\sim 10^3 e$. The size of fractal aggregates is an order of magnitude larger and, obviously, they can accumulate a charge an order of magnitude larger as well.

The role of the ionisation state of a medium in the formation of fractal clusters inside an ensemble of oppositely charged particles was considered in papers [94, 95]. It was found that, at the earlier stage of coagulation, the next step after the formation of one-, two-, and three-particle charged aggregates was the accumulation of linear structures and their joining to form branched objects. The folding of a chain to a compact structure prevents the repulsion between particles with charge of the same sign. At the later stages of the process, a directional coagulation appears, in which the contacting clusters are coupled through their oppositely charged sites. The fractal aggregates produced in this process have a lower packing density and a lower fractal dimensionality ($d_f = 1.38 \pm 0.04$ [95]).

8. Percolation in a laser plume

Both macroscopic and microscopic percolation models can be realised in a dense vapour. In the first case, the structural elements are compact clusters, and in the second – vapour atoms or molecules, which form chemical bonds due to the overlap of valence shells [96]. At the percolation threshold (at some density of structural elements), an infinite (critical) cluster appears. The microscopic percolation model well interprets the metal-dielectric transition, which is observed when the metal vapour density is close to the critical value [97]. To obtain the corresponding state using laser ablation, laser power densities of the order of 10^9 W cm^{-2} and higher are required [98]. However, if structural elements (for example, macromolecules or gas-like clusters) have the shape of oblong ellipsoids, then their threshold concentration can be substantially lower [89, 99].

Usually, the threshold dependence of the conductivity on the medium composition corresponds to percolation. The conductivity is low below the threshold; an increase in the conductivity in the vicinity of the threshold for formation of an infinite percolation cluster is characterised by a critical exponent of the order of unity; and the conductivity tends to a constant value well above the threshold. To study percolation based on this dependence, it is necessary to change the concentration of a conducting component in a broad range. Upon laser irradiation of one-component compounds, problems appear in the measurements of the absolute density of a plume and its control, for example, by varying the power density and external pressure. Another, simpler and more convenient method is the use of a two-component target, where, along with a percolating material, which is, as a rule, a metal or its oxide, also a diluent is contained.

Targets used in papers [100–105] were pressed tablets prepared from the mixtures of powdered materials. The characteristic percolation dependences were observed for the emission and microwave conductivity of a plume induced by moderate-intensity laser radiation. The percolation threshold p_c was expressed in terms of the relative concentration of atoms of the percolating component. For most mixtures studied in papers [100–104], the percolation threshold $p_c = 0.55 \pm 0.05$ was the same within the experimental error, which corresponds to the two-dimensional percolation model. Such a large threshold seems unexpected because it should not exceed 0.33 for a three-dimensional object such as a homogeneous plasma [106].

Experimental dependences were explained in [104] using the model of macroscopic percolation, in which condensate microparticles are the elements of a percolation cluster. To estimate the size of particles at specified temperature, pressure, and the diameter of a vapour–gas jet, the empirical scaling parameter (Hagena parameter)

$$\Gamma^* = \left(N r_{ch}^3\right)\left(\frac{d}{r_{ch}}\right)^q \left(\frac{T}{T_{ch}}\right)^{0.25q-1.5}, \qquad r_{ch} = \left(\frac{m}{\rho}\right)^{1/3}, \tag{11}$$

was introduced in [107–109]. Here, d is the diameter of a plasma beam with temperature T; ρ is the density of clusters; T_{ch} is the sublimation energy in kelvins; and $q = 0.85$ is a fitting parameter. According to [108], cluste-

ring in free jets begins when the Hagena parameter is ~ 200, while the developed clustering with the number of atoms of about 100 takes place when $\Gamma^* \sim 1000$.

The efficiency of clustering increases in the atmosphere of a buffer gas, which takes the excess energy released upon condensation. As pointed out in [41], the Hagena parameter is in fact the ratio of the condensation rate to the gas-flow expansion rate. Therefore, when vapour is cooled by expanding in the buffer-gas atmosphere ($P = 1$ atm), the parameter, defined by expression (11), describes condensation only qualitatively. The dependence of the Hagena parameter on the target composition was calculated in [104]. It was found that the Hagena parameter at the percolation threshold for three different mixtures ($Mo_x Al_{1-x}$, $Nb_x Mg_{1-x}$ and $(Al_2O_3)_x Al_{1-x}$), studied in the paper is $\Gamma^*_{per} \simeq 400$. In the case of a free expansion, the content of matter in a condensed fraction amounts to 30 % – 50 % [41]. The efficiency of condensation in the buffer-gas atmosphere rises and the amount of a condensate increases.

When the size of compact microclusters is lower than 1 nm (less than 1000 atoms), the average distance between them will be small compared to the Debye radius r_D. It was assumed in [104] that an additional conductivity in an ensemble of microclusters appears when the average distance between them becomes comparable with the characteristic scale r_D of the spatial inhomogeneity of plasma around an individual cluster. Due to the overlap of Debye spheres, a fractal percolation cluster is formed, which causes noticeable changes in the transport and optical properties of the plasma compared to the case when microclusters are not coupled with each other.

The percolation model adequately describes the experimental results obtained in paper [105], where the electric-dipole and magnetic-dipole absorption of microwave radiation in a plasma plume was studied. Analysis performed in [105] shows that the ratio $s = K_H/K_E$, where K_E and K_H are the efficiencies of excitation of the conduction and eddy currents in the laser plasma, does not correspond to the assumption about the plasma homogeneity in the plume. Branched fractal structures, in particular, percolation structures, which are formed when the concentration of microparticles in a laser plume is sufficiently high, can substantially affect electric-dipole and magnetic-dipole absorption because these structures contain both linear and ring fragments. The type of distribution of matter in a fractal cluster causes the efficient decrease in the conductivity with increasing cluster radius, resulting in the increase in electric-dipole absorption, whereas magnetic-dipole absorption increases due to the dominating contribution from a factor depending on the cluster size.

According to [110], the electric-dipole and magnetic-dipole absorption in a three-dimensional fractal cluster is enhanced compared to the case of isolated particles by factors of $(r_{cl}/a)^{5(3-d_f)/2}$ and $(r_{cl}/a)^{(1+d_f)/2}$, respectively. Therefore, the ratio s will increase if the fractal dimensionality exceeds 7/3, which is satisfied in the three-dimensional case for a percolation cluster ($d_f = 2.5$).

Fig. 1 shows the evolution of the ratio of magnetic-dipole and electric-dipole absorptions in a laser plume plasma studied in paper [105]. After the beginning of evaporation ($t = 0$), the ration s for targets made of various materials monotonically increases, as a rule, and then stabilises at some level after the establishment of the evaporation regime. It is obvious that the initial stage of the kinetics reflects the increase in the vapour density. Note that in the size r_f of the plume in the developed evaporation regime remains unchanged and is determined by the effect of self-focusing of laser radiation in the plasma plume. The buffer-gas pressure P was selected to provide the absence of skin effect in the plasma plume. The initial ratio was $s \sim 0.01$, which corresponds to the model of absorption in a homogeneous plasma flow having the plume size [104]. Note that the close ratio is also observed for microwave absorption signals corresponding to a thermal emission flux from the surface of some metals (for example, copper and aluminium) heated by light beams before its evaporation.

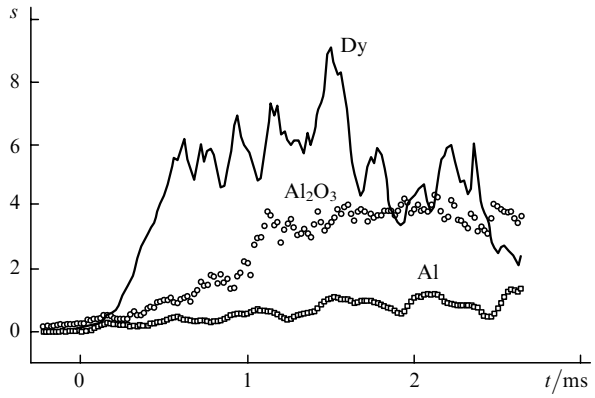

Figure 1. Dependences of the parameter $s = K_H/K_E$ on time upon laser irradiation of targets made of different materials: Dy ($r_f = 1.2$ mm, $P = 0.7$ kPa), Al_2O_3 (1.65 mm, 2 kPa), Al (3.9 mm, 7 kPa). Buffer gas is air. The instant of time $t = 0$ corresponds to the beginning of evaporation; r_f is the size of the laser plume.

9. Efficiency of fractal formation

The efficiency of fractal formation as a function of the buffer-gas pressure was studied in paper [111]. It was found that this dependence observed during laser evaporation has a distinct maximum at some pressure P_1, which is mainly determined by the target material. The efficiency decreases with increasing pressure simultaneously with a decrease in the laser plume length. The plasma expansion is limited not only due to the counterpressure exerted by the buffer gas but also due to the presence of a certain connectivity in cooled plume layers or in the plasma itself, as follows from the decisive role of the target material. In the pressure range below P_1, the developed evaporation regime takes place, which is characterised by the expansion of the erosion plasma appearing near the target surface, where its temperature is close to the boiling temperature. At pressures P_2 exceeding P_1, the emission of the plume drastically increases. Such a behaviour is observed due to a change in the regime of flame propagation: the expansion of the erosion plasma passes to a considerably more bright light combustion in a vapour – gas flow containing a finely divided phase. The dependence of the emission intensity of pressure has a threshold. The emission reaches a maximum when the discharge region is pressed down to the target surface and virtually completely screens the target from laser radiation. If the target is burnt through, the discharge disappears and emission decays with the characteristic time $t \leqslant 10^{-3}$ s.

It was found in [111] that the decrease in the efficiency of fractal formation is accompanied by the combination of fractal aggregates within the shell at the periphery of the erosion plume, which also restricts the energy and diffusion losses in the plasma volume. The fractal shell was observed in experiments in the form a compact folded network structure. The mechanisms of its formation and destruction, as well as its influence on the plume parameters were considered in detail in paper [111]. The shell appears after the following sequence of processes: (1) the condensation of vapour with the formation of compact clusters; (2) the ejection of clusters by a thermophoretic force to the periphery of the laser plume; (3) the retardation of clusters by the Stokes force and their accumulation in some layer surrounding the discharge plasma; and (4) the aggregation to weakly coupled microclusters at low densities of the evaporated material or (when some critical density of particles is exceeded) to a strongly bound macroscopic fractal structure (shell). The behaviour of the laser-plume plasma with a finely divided phase is similar in many respects to that of the dusty plasma and is manifested in the threshold nature of the appearance of an internal cavity with distinct boundaries and enhanced emission [45, 46].

Fig. 2 shows the dependences of the efficiency of fractal formation and the emission intensity of the plasma cloud near the target surface on the buffer-gas pressure for some metals from three different groups of the Periodic table of elements. Note first of all the fact that the positions of the characteristic points (the maximum on the curve of fractal formation and the drop in the brightness temperature), which weakly change within each separate group, noticeably shift in passing from one group to another. The exclusion are the elements of the rare-earth group, for which the position of the maximum of fractal formation considerably shifts in passing from one element to another. Note in this connection that the external shells of rare-earth elements have different structures [112].

The dependences of pressures P_1 and P_2 averaged within a group of the Periodic system on the group number are presented in Fig. 3. The so-called long form of the Periodic system is used in which subgroups are absent and all the elements having the same structure of external electron shells are assigned to one group [113]. The curve drawn for clarity shows that the periodicity of the Mendeleev Periodic

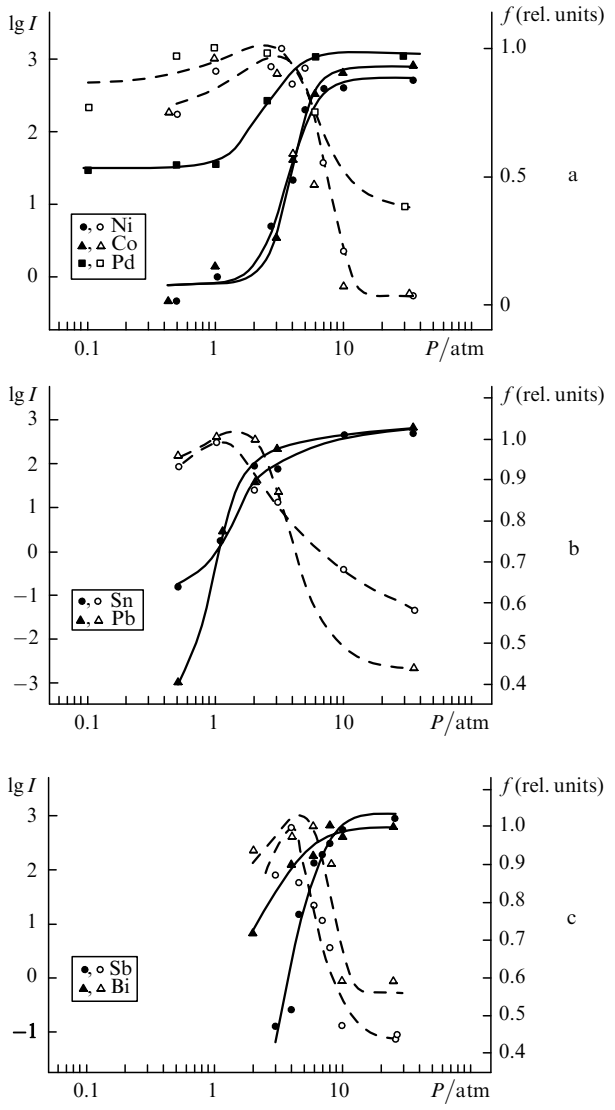

Figure 2. Dependences of the normalised emission intensity I of a laser plume at a wavelength of 0.47 μm (dark symbols) and the efficiency of fractal formation (light symbols) on the pressure P of a buffer argon gas for metals of the eighth (a), twelfth (b), and thirteenth (c) groups.

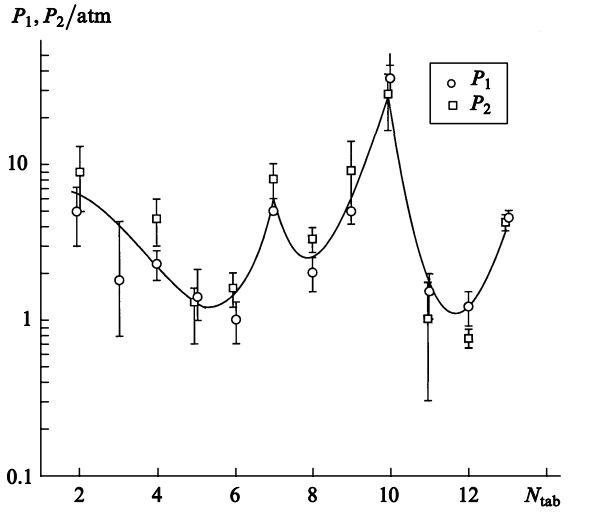

Figure 3. Pressures corresponding to the maximum of fractal formation (P_1) and to the intensity jump (P_2) for different groups of the Periodic system (N_{tab} is the group number).

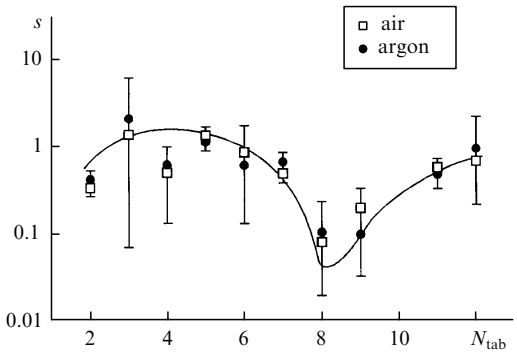

Figure 4. Dependences of the ratio $s = K_H/K_E$ on the number N_{tab} of the group of the Periodic system. Buffer gases are air and argon at a pressure of $\sim$ 100 Torr.

table is manifested in these experimental dependences. Fig. 4 presents the results of measurements of the ratio between the electric-dipole and magnetic-dipole absorptions in the erosion plasma at the initial stage of the laser-plume development. Here, chemical elements of the same group, belonging to different periods, are also characterised by close values of s (except, rare-earth elements, as above).

Note that the relation between the characteristics of the optical breakdown plasma and the electronic structure of target atoms was first found in paper [114], where a change in the regime of plasma ejection above a threshold density of the radiation flux was studied, and variations in this threshold for metals arranged in sequence in the Periodic table were observed.

It is clear that the characteristics of both microscopic structures and macroscopic objects should depend on the electronic sructure. For example, the ionisation potential, the melting temperature, the latent evaporation heat, the electric conduction, the work function, and other parameters of metals possess a periodicity, similar to that observed in Figs 3 and 4. Such a periodicity of these dependences is difficult to explain using the model of diffusion-restricted aggregation of compact particles, according to which the electronic structure of chemical elements should not play an important role. On the contrary, the strength of coupling in a structure formed from gas-like molecular clusters is determined by the valence shell of a particular element.

10. Formation of linear structures

Fractal structures deposited on a cover glass upon laser evaporation of an iron target were studied with a scanning electron microscope [111]. Figs 5 and 6 show the fragments of microphotographs taken from [111]. The analysis of the microstructure of fractal layers suggests that the objects under study consist of 'nanowire' fragments and chains of spheres rather than of separate compact particles. At pressures $P < P_1$, fractal structures deposited on a substrate contain linear fragments of length ~ 1 μm and diameter ~ 50 nm (Fig. 5). Along a fragment, a weak thinner structure can be often observed with a characteristic size ~ 50 nm. As the pressure of the buffer gas is increased ($P > P_1$), the characteristic diameter and length of fragments are doubled approximately. In addition, separate frozen drops of size 200 – 500 nm appear in deposited layers, and then chains consisting of 10 – 20 drops of the same size (Fig. 6). Fig. 7 shows the two-point correlation function [115]

$$g(r) \propto \frac{N_g(r)}{\pi r^2} \tag{12}$$

for the fractal structure shown in Fig. 5. Here, $N_g(r)$ is the average number of points at the distance r from any chosen point of an image being analysed. The break in the curve, beginning at $r = 3$ μm, is caused by a finite size of the image. The correlation function for fractal two-dimensional structures, as shown in paper [116], has the form

$$g(r) \propto r^{d_f - 2}, \; r < \xi, \tag{13}$$

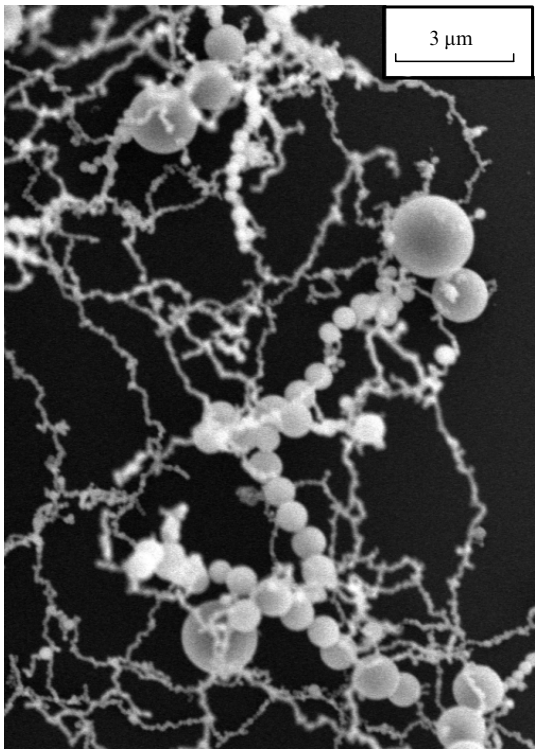

Figure 6. Electron microscope photography of a fractal layer deposited upon evaporation of an iron target in the vapour discharge regime.

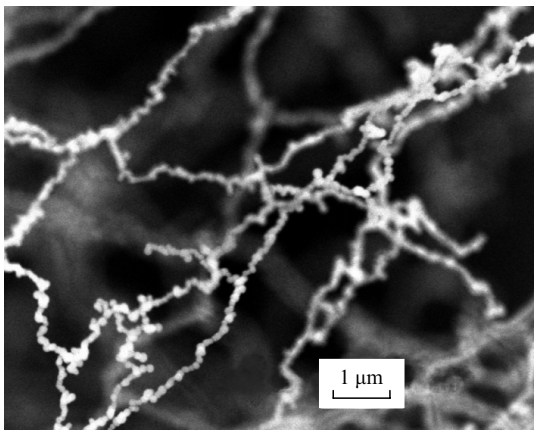

Figure 5. Electron microscope photography of a fractal layer deposited upon evaporation of an iron target in the erosion plume regime.

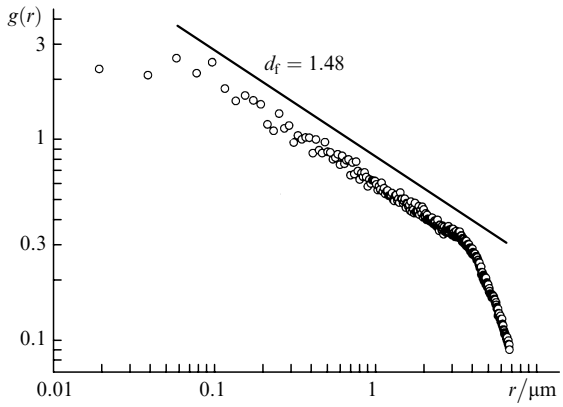

Figure 7. Two-point correlation function (circles) for the object shown in Fig. 5 and its approximation for $d_f = 1.48$ (solid straight line).

where ξ is the correlation length, which is equal approximately to the pore size in the structure. The zero slope for $r < 100$ nm gives the dimensionality $d_f = 2$, which corresponds to compact particles. At the interval from 100 nm to 3 μm, a linear dependence is observed at a double logarithmic scale, corresponding to $d_f = 1.48$. The Hausdorff dimensionality calculated by the cell method for this structure is 1.62. A lower correlation dimensionality can be caused by the multifractality [117].

As pressure increases, the fractal dimensionality and thickness of a fractal layer decrease, while the size of separate clusters and of separate fragments of the structure increases. Such behaviour and the appearance of drops are explained by the melting of the fractal structure in contact with the optical discharge plasma. At pressures far exceeding P_1, instead of a layer of branched fractals, many droplets of diameter ~ 1 μm are observed on a cover glass.

We mentioned in Section 7 that chains are formed in the presence of dipole interaction between subunits. The parameter characterising the probability of the appearance of chains is determined by expression (10). The dependence of the average $\langle L_0 \rangle$ number of links in the dipole chain on the parameter p^* and the volume fraction $\Psi \ll 1$ per dipole particles has the form [118]

$$\langle L_0 \rangle = \sqrt{\Psi} \exp\left[p^* \coth(2p^*)\right]. \quad (14)$$

When the parameter $p^* \approx 4$ and the volume fraction $\Psi \approx 0.2$, which corresponds approximately to the percolation threshold, then, according to (14), the parameter $\langle L_0 \rangle \approx 20$. Therefore, if the model is valid for the chains of iron drops, the energy of dipole–dipole interaction between separate particles (droplets) exceeds the thermal energy by a factor of four.

Similar chains were observed upon the deposition of vapours of the iron-cobalt alloy on a substrate at temperature below the Curie temperature [119]. Compact clusters of diameter ~ 35 nm deposited from a vapour phase acquired a considerable magnetisation after cooling on a substrate. By moving over the substrate surface, they form chains of magnetic dipoles. It is obvious that induced electric dipoles play a dominant role in experiments [111] because chains were observed not only for ferromagnetic metals but also for vanadium, manganese, lead, and other low-melting elements. Moreover, chains appear in the hot plasma. When fractal aggregates are irradiated by a laser, the chains, which existed before, melt and new chains of droplets appear.

It is reasonable to assume that, first, the chains are formed at temperatures that are lower than the melting temperature of the metal and, second, the dipoles are induced by slowly varying electric fields in plasma. Despite extensive studies, the picture of electromagnetic phenomena in laser plasmas remains unclear. The density and temperature gradients produce the charge separation and electric fields in plasma [45, 77, 120, 121]. Near the surface of various media and at the plasma boundaries, a double electrical layer appears. A slowly varying electric field, whose potential can achieve 10–100 V, appears near the surface of bodies surrounding a laser plume due to photoeffect caused by the short-wavelength plasma radiation [122]. The latter can affect the charge of particles in the dispersion phase and also induce an electric dipole moment in the compact particle-electron cloud system, if the irradiation of the system is not symmetric.

Assuming that the energy of dipole–dipole interaction exceeds the energy of thermal motion ($T \approx 2000$ K) by a factor four, we obtain the electric dipole moment for interacting particles of radius ~ 50 nm equal to 2×10^3 D. Such a dipole moment can be obtained for comparatively small charges and large particles. Note that the charge of a dusty particle of this size in a thermal plasma can achieve $\sim 10^2 e$ [123].

11. Conclusions

Upon evaporation of various particles by laser radiation, a finely divided phase is formed in a plasma plume due to vapour condensation. The plasma produced upon irradiation of condensed media by moderate-intensity light fluxes is an efficient source of fractals, both microscopic and macroscopic. The experimental study of the formation of fractals presented in this paper has shown that these processes occur in the plasma volume and depend on the electronic structure of the target atoms. At high pressures, a macrofractal shell appears, which surrounds the laser plume and is formed at several stages. First gas-like clusters (molecular associates) appear in the laser radiation field, which form compact clusters during collisions. The latter move to the plume periphery because of the temperature gradient, where, acquiring the electric dipole moment due to photoeffect, they first combine to form chains and then to form a network shell (macrofractal).

The electron microscope images of fractal objects suggest that nanowire fragments are main elements of cooled microscopic and macroscopic structures. At high pressures, a fragment heated up to the melting temperature is folded to form a drop. The drops are combined to form linear chains due to the dipole–dipole interaction.

References

1. Zhukhovitskii D.I. *Zh. Eksp. Teor. Fiz.*, **113**, 181 (1998).
2. Zhukhovitskii D.I. *Zh. Eksp. Teor. Fiz.*, **121**, 396 (2002).
3. Kukushkin A.B., Rantsev-Kartinov V.A. *Laser and Part. Beams*, **16**, 445 (1998).
4. Afanas'ev Yu.V., Krokhin O.N. *Zh. Eksp. Teor. Fiz.*, **52**, 966 (1967).
5. Anisimov S.I., Imas Ya.A., Romanov G.S., Khodyko Yu.V. *Deistvie izlucheniya bol'shoi moshchnosti na metally* (Effect of High-Power Radiation on Metals) (Moscow: Nauka, 1970).
6. Ready J.F. *Effects of High-Power Laser Radiation* (New York: Academic Press, 1971; Moscow: Mir, 1974).
7. Batanov V.A., Bunkin F.V., Prokhorov A.M., Fedorov V.B. *Zh. Eksp. Teor. Fiz.*, **63**, 586 (1972).
8. Uglov A.A., Kokora A.N. *Kvantovaya Elektron.*, **4**, 1189 (1977) [*Sov. J. Quantum Electron.*, **7**, 671 (1977)].
9. Vedenov A.A., Gladush G.G. *Fizicheskie protsessy pri lazernoi obrabotke metallov* (Physical Processes in Laser Machining of Metals) (Moscow: Energoatomizdat, 1985).
10. Samokhin A.A. *Trudy IOFAN*, **13**, 3 (1988).
11. Lyubov B.Ya., Sobol' E.N., in *Deistvie kontsentrirovannykh potokov energii na materialy* (Effect of Concentrated Energy Fluxes on Materials) (Moscow: Nauka, 1985) p. 226.
12. Anisimov S.I., Luk'yanchuk B.S. *Usp. Fiz. Nauk*, **172**, 301 (2002).
13. Brykin M.V., Vorob'ev V.S., Shelyukhaev V.P. *TVT*, **25**, 468 (1987).
14. Dan'shchikov E.V., Lebedev F.V., Ryazanov A.V. *Fiz. Plazm.*, **10**, 385 (1984).

15. Dan'shchikov E.V., Dymshakov V.A., Lebedev F.V., et al. *Kvantovaya Elektron.*, **12**, 1863 (1985) [*Sov. J. Quantum Electron.*, **15**, 1231 (1985)].
16. Zaikin A.E., Levin A.V., Petrov A.L. *Kvantovaya Elektron.*, **22**, 145 (1995) [*Quantum Electron.*, **25**, 135 (1995)].
17. Bulgakov A.V., Bulgakova N.M. *Kvantovaya Elektron.*, **27**, 154 (1999) [*Quantum Electron.*, **29**, 433 (1999)].
18. Goncharov V.K., Kontsevoi V.L., Puzyrev M.V. *Kvantovaya Elektron.*, **22**, 249 (1995) [*Quantum Electron.*, **25**, 232 (1995)].
19. Goncharov V.K., Puzyrev M.V. *Kvantovaya Elektron.*, **24**, 329 (1997) [*Quantum Electron.*, **27**, 319 (1997)].
20. Anisimov S.I., Grishina V.G., Dergach O.N., et al. *Kvantovaya Elektron.*, **22**, 815 (1995) [*Quantum Electron.*, **25**, 784 (1995)].
21. Akhmanov S.A., Emel'yanov V.I., Koroteev N.I., Seminogov V.N. *Usp. Fiz. Nauk*, **147**, 675 (1985).
22. Barchukov A.I., Bunkin F.V., Konov V.I., Prokhorov A.M. *Pis'ma Zh. Eksp. Teor. Fiz.*, **17**, 413 (1973).
23. Bonch-Bruevich A.M., Kaporskii L.N., Romanenkov A.A. *Zh. Tekh. Fiz.*, **43**, 1746 (1973).
24. Barchukov A.I., Bunkin F.V., Konov V.I., Lyubin A.A. *Zh. Eksp. Teor. Fiz.*, **66**, 965 (1974).
25. Kovalev A.S., Popov A.M., Rakhimov A.T., et al. *Kvantovaya Elektron.*, **12**, 713 (1985) [*Sov. J. Quantum Electron.*, **15**, 468 (1985)].
26. Walters C.T. *Appl. Phys. Lett.*, **25**, 695 (1974).
27. Nielson P.E. *Appl. Phys. Lett.*, **27**, 458 (1975).
28. Kovalev A.S., Popov A.M. *Zh. Tekh. Fiz.*, **50**, 333 (1980).
29. Bunkin F.V., Konov V.I., Prokhorov A.M., Fedorov V.B. *Pis'ma Zh. Eksp. Teor. Fiz.*, **9**, 609 (1969).
30. Raizer Yu.P. *Osnovy sovremennoi fiziki gazorazryadnykh protsessov* (Foundations of the Modern Physics of Gas-Discharge Processes) (Moscow: Nauka, 1980).
31. Bakeev A.A., Nikolashina L.I., Prokopenko N.V. *Kvantovaya Elektron.*, **7**, 1236 (1980) [*Sov. J. Quantum Electron.*, **10**, 708 (1980)].
32. Rykalin N.N., Uglov A.A., Nizametdinov M.M. *Dokl. Akad. Nauk SSSR*, **218**, 330 (1974).
33. Rykalin N.N., Uglov A.A., Dobrovol'skii I.P., Nizametdinov M.M. *Kvantovaya Elektron.*, **1**, 1928 (1974) [*Sov. J. Quantum Electron.*, **4**, 1068 (1974)].
34. Rykalin N.N., Uglov A.A., Nizametdinov M.M. *Zh. Eksp. Teor. Fiz.*, **69**, 722 (1975).
35. Tsytovich V.N. *Aust. J. Phys.*, **51**, 763 (1998).
36. Morfill G.E. *Phys. Plasma*, **6**, 1 (1999).
37. Smirnov B.M. *Usp. Fiz. Nauk*, **170**, 495 (2000).
38. Smirnov B.M. *Fiz. Plazmy*, **34**, 512 (1996).
39. Echt O., Sattler K., Recknagel E. *Phys. Rev. Lett.*, **47**, 1121 (1981).
40. Landau L.D., Lifshits E.M. *Statisticheskaya fizika* (Statistical Physics) (Moscow: Fizmatlit, 2001).
41. Smirnov B.M. *Usp. Fiz. Nauk*, **164**, 665 (1994).
42. Mikhailov E.F., Vlasenko S.S. *Usp. Fiz. Nauk*, **165**, 263 (1995).
43. Ikezi H. *Phys. Fluids*, **29**, 1764 (1986).
44. Chu J.H., Lin I. *Phys. Rev. Lett.*, **72**, 4009 (1994).
45. Samsonov D., Goree J. *Phys. Rev. E*, **59**, 1047 (1999).
46. Thomas H., Morfill G.E. *Phys. Rev. Lett.*, **73**, 652 (1994).
47. Fortov V.E., Nefedov A.P., Torchinskii V.M., et al. *Pis'ma Zh. Eksp. Teor. Fiz.*, **64**, 86 (1996).
48. Howling A.A., Sansonnens A., Dorier J.-L., Hollenstein Ch. *J. Appl. Phys.*, **75**, 1340 (1994).
49. Stoffels E., Stoffels W.W., Kroesen G.M.W., de Hoog F.J. *J. Vac. Sci. Technol. A*, **14**, 556 (1996).
50. Boufendi L., Bouchoule A. *Plasma Sourse Sci. Technol.*, **3**, 262 (1994).
51. Sidorov L.N., Korobov N.V., Zhuravleva L.V. *Mass-spektral'nye termodinamicheskie issledovaniya* (Mass-spectroscopy Thermodynamic Studies) (Moscow: Izd. Moscow State University, 1985).
52. Zel'dovich Ya.B., Raizer Yu.P. *Fizika udarnykh voln i vysokotemperaturnykh gidrodinamicheskikh yavlenii* (Physics of Shock Waves and High-Temperature Hydrodynamic Phenomena) (Moscow: Nauka, 1966).
53. Semenov G.A., Stolyarova V.L. *Mass-spectrometricheskie issledovaniya ispareniya oksidnykh sistem* (Mass-spectroscopy Studies of Evaporation of Oxide Systems) (Leningrad: Nauka, 1990).
54. Berkowitz J., Chupka W.A. *J. Chem. Phys.*, **40**, 2735 (1964).
55. Rohlfing E.A., Cox D.M., Caldor A. *J. Chem. Phys.*, **81**, 3322 (1984).
56. Kroto H.W., Health J.R., O'Brien S.C., et al. *Nature*, **318**, 162 (1985).
57. Aubriet F., Chaoui N., Chety R., Maunit B., et al. *Appl. Surf. Sci.*, **186**, 282 (2002).
58. Eletskii A.V. *Usp. Fiz. Nauk*, **172**, 401 (2002).
59. Scott C.D., Arepalli S., Nikolaev P., Smalley R.E. *Appl. Phys. A*, **72**, 573 (2001).
60. Anisimov S.I., Luk'yanchuk B.S. *Usp. Fiz. Nauk*, **172**, 301 (2002).
61. Raizer Yu.P. *Zh. Eksp. Teor. Fiz.*, **37**, 1229 (1960).
62. Luk'yanchuk B.S., Marine W., Anisimov S.I., Simakina G.A. *Proc. SPIE Int. Soc. Opt. Eng.*, **3618**, 434 (1999).
63. Kuwata M., Luk'yanchuk B.S., Yabe T. *Proc. SPIE Int. Soc. Opt. Eng.*, **4065**, 441 (2000).
64. Marine W., Luk'yanchuk B.S., Sentis M. *Le Vide Sci. Tech. Appl.*, **288**, 440 (1998).
65. Movtchan I.A., Marine W., Dreyfus R.W., et al. *Appl. Surf. Sci.*, **96-98**, 251 (1996).
66. Geohegan D.B., Puretzky A.A., Duscher G., Pennycook S.J. *Appl. Phys. Lett.*, **72**, 2987 (1998).
67. Rosenbauer M., Finkbeiner S., Bustarret E., et al. *Phys. Rev. B*, **51**, 10539 (1995).
68. Muramoto J., Inmaru T., Nakata Y., et al. *Appl. Phys. Lett.*, **77**, 2334 (2000).
69. Lushnikov A.A., Pakhomov A.V., Chernyaeva G.A. *Dokl. Akad. Nauk SSSR*, **292**, 86 (1987).
70. Lushnikov A.A., Negin A.E., Pakhomov A.V. *Chem. Phys. Lett.*, **175**, 138 (1990).
71. Cui C., Goree J. *IEEE Trans. Plasma Sci.*, **49**, 4430 (1994).
72. Khodataev Y.K., Khrapak S.A., Nefedov A.P., Petrov O.F. *Phys. Rev. E*, **57**, 7086 (1998).
73. Forrest S.R., Witten T.A. *J. Phys. A*, **12**, L109 (1979).
74. Niklasson G.A., Granqvist C.G. *Phys. Rev. Lett.*, **56**, 256 (1986).
75. Martin J.E. *Phys. Rev. A*, **36**, 3415 (1987).
76. Kask N.E., Fedorov G.M. *Kvantovaya Elektron.*, **20**, 527 (1993) [*Quantum Electron.*, **23**, 423 (1993)].
77. Samsonov D., Goree J. *J. Vac. Sci. Technol. A*, **17**, 2835 (1999).
78. Smirnov B.M. *Usp. Fiz. Nauk.*, **149**, 177 (1986).
79. Kolb M., Botet R., Jullien R. *Phys. Rev. Lett.*, **51**, 1123 (1983).
80. Jullien R., Kolb M. *J. Phys. A*, **17**, L639 (1984).
81. Stauffer D., Coniglio A., Adam M. *Adv. Polym. Sci.*, **44**, 103 (1982).
82. Smirnov B.M. *Phys. Rep.*, **188**, 1 (1990).
83. Weis J.J., Levesque D. *Phys. Rev. Lett.*, **71**, 2729 (1993).
84. Pastor-Satorras R., Rubi J.M. *Phys. Rev. E*, **51**, 5994 (1995).
85. Tan Z.-J., Zou X.-W., Zhang W.-B., Jin Z.-Z. *Phys. Rev. E*, **62**, 734 (2000).
86. Sancho M., Giner V., Martinez G. *Phys. Rev. E*, **55**, 544 (1997).
87. Niklasson G.A., Torebring A., Larsson C., Granqvist C.G. *Phys. Rev. Lett.*, **60**, 1735 (1988).
88. Jensen P. *Rev. Mod. Phys.*, **71**, 1695 (1999).
89. Aleksashenko V.A., Ivlev L.S., Ponomarev N.G., et al. *Vestn. Leningr. Univ.*, Ser. 4, (3), 32 (1987).
90. Kistler S.S. *J. Chem. Phys.*, **39**, 79 (1935).
91. Freltoft T., Kjems J.K., Sinha S.K. *Phys. Rev. B*, **33**, 269 (1990).
92. Jensen P. *Phys. Rev. B*, **50**, 15316 (1994).
93. Pastor-Satorras R. *Phys. Rev. Lett.*, **80**, 5373 (1998).
94. Vorontsov-Vel'yaminov P.N., Shevkunov S.V. *Fiz. Plazmy*, **4**, 1354 (1978).
95. Mikhailov E.F., Vlasenko S.S., Kiselev A.A. *Fiz. Plazmy*, **21**, 442 (1995).
96. Likal'ter A.A. *Usp. Fiz. Nauk*, **162**, 119 (1992).
97. Likalter A.A. *Phys. Rev. B*, **53**, 1602 (1996).
98. Bulgakova N.M., Bulgakov A.V. *Appl. Phys. A*, **73**, 199 (2001).
99. Manykin E.A., Ozhovan M.I., Poluektov P.P. *Zh. Eksp. Teor. Fiz.*, **84**, 442 (1983).
100. Kask N.E. *Pis'ma Zh. Eksp. Teor. Fiz.*, **60**, 204 (1994).

101. Kask N.E. *Kvantovaya Elektron.*, **21**, 805 (1994) [*Quantum Electron.*, **24**, 747 (1994)].
102. Kask N.E., Fedorov G.M. *Kvantovaya Elektron.*, **23**, 1033 (1996) [*Quantum Electron.*, **26**, 1007 (1996)].
103. Kask N.E., Michurin S.V., Fedorov G.M., et al. *Kvantovaya Elektron.*, **25**, 951 (1998) [*Quantum Electron.*, **28**, 926 (1998)].
104. Kask N.E., Michurin S.V., Fedorov G.M. *TVT*, **37**, 9 (1999).
105. Kask N.E., Michurin S.V., Fedorov G.M. *Zh. Eksp. Teor. Fiz.*, **116**, 1979 (1999).
106. Clerc J.P., Girand G., Laugier J.M., Luck J.M. *Adv. Phys.*, **39**, 443 (1990).
107. Hagena O.F. *Surf. Sci.*, **106**, 101 (1981).
108. Hagena O.F. *Zs. Phys. D*, **4**, 291 (1987).
109. Hagena O.F. *Rev. Sci. Instr.*, **63**, 2374 (1992).
110. Hui P.M., Stroud D. *Phys. Rev. B*, **33**, 2163 (1986).
111. Kask N.E., Leksina E.G., Michurin S.V., et al. *Kvantovaya Elektron.*, **32**, 437 (2002) [*Quantum Electron.*, **32**, 437 (2002)].
112. Khomskii D.I. *Usp. Fiz. Nauk*, **129**, 443 (1979).
113. Kikoin I.K. (Ed.) *Tablitsy fizicheskikh velichin. Spravochnik* (Handbook of Physical Quantities) (Moscow: Atomizdat, 1976).
114. Gaponov S.V., Luchin V.I., Stikovskii M.D. *Pis'ma Zh. Eksp. Teor. Fiz.*, **6**, 1409 (1999).
115. Peebles P.J.E. *The Large Scale Structure of the Universe* (Princeton, New Jersey: Princeton University Press, 1980).
116. Martin J.E. *J. Phys. A*, **18**, L207 (1985).
117. Halsey T.C., Jensen M.H., Kadanoff L.P., Procaccia I., Shraiman B.I. *Phys. Rev. A*, **33**, 1141 (1986).
118. Huang J.-Y., Lay P.-Y. *Chinese J. Phys.*, **38**, 962 (2000).
119. Gangopadhyay S., Yang Y., Hadjipanayis G.C. *J. Appl. Phys.*, **76**, 6319 (1994).
120. Dement'ev D.A., Konov V.I., Nikitin P.I., Prokhorov A.M. *Kvantovaya Elektron.*, **8**, 1532 (1981) [*Sov. J. Quantum Electron.*, **11**, 923 (1981)].
121. Kabashin A.V., Nikitin P.I., Marine V., Sentis M. *Kvantovaya Elektron.*, **25**, 26 (1998) [*Quantum Electron.*, **28**, 24 (1998)].
122. Barchukov A.I., Konov V.I., Nikitin P.I., Prokhorov A.M. *Zh. Eksp. Teor. Fiz.*, **78**, 957 (1980).
123. Fortov V.E., Nefedov A.P., Petrov O.E., Samarian A.A., et al. *Pis'ma Zh. Eksp. Teor. Fiz.*, **63**, 176 (1996).